A&A 611, A29 (2018)
DOI: 10.1051/0004-6361/201732038

Astronomy & Astrophysics

Abundance of SiC_2 in carbon star envelopes*

Evidence that SiC_2 is a gas-phase precursor of SiC dust

S. Massalkhi[1], M. Agúndez[1], J. Cernicharo[1], L. Velilla Prieto[1], J. R. Goicoechea[1], G. Quintana-Lacaci[1], J. P. Fonfría[1], J. Alcolea[2], and V. Bujarrabal[3]

[1] Grupo de Astrofísica Molecular, Instituto de Ciencia de Materiales de Madrid, CSIC, C/ Sor Juana Inés de la Cruz 3, 28049 Cantoblanco, Spain
e-mail: sarah.massalkhi@csic.es
[2] Observatorio Astronómico Nacional (IGN), C/ Alfonso XII 3, 28014 Madrid, Spain
[3] Observatorio Astronómico Nacional (IGN), Apartado de Correos 112, 28803 Alcalá de Henares, Madrid, Spain

Received 4 October 2017 / Accepted 27 October 2017

ABSTRACT

Context. Silicon carbide dust is ubiquitous in circumstellar envelopes around C-rich asymptotic giant branch (AGB) stars. However, the main gas-phase precursors leading to the formation of SiC dust have not yet been identified. The most obvious candidates among the molecules containing an Si–C bond detected in C-rich AGB stars are SiC_2, SiC, and Si_2C. To date, the ring molecule SiC_2 has been observed in a handful of evolved stars, while SiC and Si_2C have only been detected in the C-star envelope IRC +10216.
Aims. We aim to study how widespread and abundant SiC_2, SiC, and Si_2C are in envelopes around C-rich AGB stars, and whether or not these species play an active role as gas-phase precursors of silicon carbide dust in the ejecta of carbon stars.
Methods. We carried out sensitive observations with the IRAM 30 m telescope of a sample of 25 C-rich AGB stars to search for emission lines of SiC_2, SiC, and Si_2C in the λ 2 mm band. We performed non-LTE excitation and radiative transfer calculations based on the LVG method to model the observed lines of SiC_2 and to derive SiC_2 fractional abundances in the observed envelopes.
Results. We detect SiC_2 in most of the sources, SiC in about half of them, and do not detect Si_2C in any source except IRC +10216. Most of these detections are reported for the first time in this work. We find a positive correlation between the SiC and SiC_2 line emission, which suggests that both species are chemically linked; the SiC radical is probably the photodissociation product of SiC_2 in the external layer of the envelope. We find a clear trend where the denser the envelope, the less abundant SiC_2 is. The observed trend is interpreted as evidence of efficient incorporation of SiC_2 onto dust grains, a process that is favored at high densities owing to the higher rate at which collisions between particles take place.
Conclusions. The observed behavior of a decline in the SiC_2 abundance with increasing density strongly suggests that SiC_2 is an important gas-phase precursor of SiC dust in envelopes around carbon stars.

Key words. astrochemistry – molecular processes – stars: abundances – stars: AGB and post-AGB – stars: carbon – circumstellar matter

1. Introduction

Low- and intermediate-mass stars, with initial masses <8 $M_\odot$, experience in their late stages of evolution known as the asymptotic giant branch (AGB), intense mass-loss processes which result in circumstellar envelopes (CSEs) made up of molecules and dust grains. AGB stars are the main sources of interstellar dust in the Galaxy (Gehrz 1989). The chemical nature of the synthesized dust is determined by the C/O elemental abundance ratio at the surface of the AGB star. Dust is mainly composed of silicates in envelopes around oxygen-rich stars (C/O < 1), while carbonaceous and silicon carbide dust is formed around carbon-rich stars (C/O > 1; e.g., Swamy 2005). The dust formation process involves a first step in which condensation nuclei of nanometer size are formed from some gas-phase precursors of highly refractory character, a process that takes place in the surroundings of the stellar atmosphere. The second step involves the growth of the nuclei to micrometer sizes by accretion and coagulation as the material is pushed out by the stellar wind (Gail et al. 1984). What the gas-phase building blocks of condensation nuclei are and how these particles evolve toward the micrometer-sized grains that populate the interstellar medium are key questions that are not yet well understood.

In this article we perform an observational study to constrain the main gas-phase precursors of silicon carbide (SiC) dust in C-rich AGB stars. The presence of SiC dust in circumstellar envelopes C-rich AGB stars was established through the observation of a solid-state emission band at ~11.3 μm (Hackwell 1972; Treffers & Cohen 1974). The 11.3 μm feature has been observed toward a large number of C-rich AGB stars with the IRAS and ISO satellites (e.g., Little-Marenin 1986; Chan & Kwok 1990; Yang et al. 2004). However, what the gas-phase precursors of SiC dust are is still a pending question.

Various molecules containing an Si−C bond have been observed in envelopes around C-rich AGB stars and are potential gas-phase precursors of SiC dust. The ring molecule SiC_2 has long been observed in the atmospheres of optically visible carbon stars through the Merrill-Sanford electronic bands (see, e.g., Sarre et al. 2000). Thaddeus et al. (1984) reported the first observation of the rotational spectrum of SiC_2 toward the highly reddened envelope IRC +10216; since then observations of this

* Based on observations carried out with the IRAM 30 m Telescope. IRAM is supported by INSU/CNRS (France), MPG (Germany), and IGN (Spain).

Table 1. Sample of carbon stars.

Name	RA J2000.0	Dec J2000.0	V_{LSR} (km s^{-1})	D (pc)	$T_\star$ (K)	$L_\star$ ($L_\odot$)	$\dot{M}$ ($M_\odot$ yr^{-1})	V_{exp} (km s^{-1})	$T_d(r_c)$ (K)	r_c (cm)	Ψ
IRC +10216	09:47:57.45	+13:16:43.9	−26.5	130 [a]	2330 [a]	8750 [a]	2.0×10^{-5} [a]	14.5	800 [a]	2.0×10^{14} [a]	300 [a]
CIT 6	10:16:02.27	+30:34:18.6	−1	440 [g]	1800 [g]	10000 [g]	6.0×10^{-6} [g]	17	1000 [g]	2.1×10^{14} [g]	141 [d]
CRL 3068	23:19:12.24	+17:11:33.4	−31.5	1300 [g]	1800 [g]	10900 [g]	2.5×10^{-5} [g]	14.5	1500 [g]	2.0×10^{14} [g]	174 [d]
S Cep	21:35:12.83	+78:37:28.2	−15.3	380 [k]	2200 [k]	7300 [k]	1.2×10^{-6} [k]	22.5	1400 [k]	5.8×10^{13} [k]	360 [d]
IRC +30374	19:34:09.87	+28:04:06.3	−12.5	1200 [j]	2000 [j]	9800 [j]	1.0×10^{-5} [j]	25	1000 [j]	2.2×10^{14} [j]	1008 [d]
Y CVn	12:45:07.83	+45:26:24.9	+22	220 [k]	2200 [k]	4400 [k]	1.5×10^{-7} [k]	7	1500 [k]	8.7×10^{13} [k]	500 [h]
LP And	23:34:27.53	+43:33:01.2	−17	630 [g]	1900 [g]	9600 [g]	7.0×10^{-6} [g]	14.5	1100 [g]	1.8×10^{14} [g]	288 [d]
V Cyg	20:41:18.27	+48:08:28.8	+13.5	366 [g]	2300 [g]	6000 [g]	1.6×10^{-6} [g]	12	1400 [g]	9.4×10^{13} [g]	364 [d]
UU Aur	06:36:32.84	+38:26:43.8	+6.7	260 [k]	2800 [k]	6900 [k]	2.4×10^{-7} [k]	10.6	1500 [k]	6.3×10^{13} [k]	11111 [b]
V384 Per	03:26:29.51	+47:31:48.6	−16.8	560 [k]	2000 [k]	8100 [k]	2.3×10^{-6} [b]	15.5	1300 [k]	1.0×10^{14} [k]	584 [d]
IRC +60144	04:35:17.54	+62:16:23.8	−48.8	1030 [b]	2000 [b]	7800 [b]	3.7×10^{-6} [b]	19.5	1200 [n]	2.0×10^{14} [b]	11 [b]
U Cam	03:41:48.17	+62:38:54.4	+6	430 [i]	2695 [i]	7000 [i]	2.0×10^{-7} [i]	13	1500 [j]	4.4×10^{13} [j]	833 [i]
V636 Mon	06:25:01.43	−09:07:15.9	+10	880 [f]	2500 [n]	8472 [e]	5.8×10^{-6} [f]	20	1200 [n]	1.7×10^{14} [n]	300 [n]
IRC +20370	18:41:54.39	+17:41:08.5	−0.8	600 [k]	2200 [k]	7900 [k]	3.0×10^{-6} [b]	14	1500 [k]	8.1×10^{13} [k]	266 [d]
R Lep	04:59:36.35	−14:48:22.5	+11.5	432 [b]	2200 [b]	5500 [b]	8.7×10^{-7} [b]	17.5	1000 [g]	1.8×10^{14} [b]	2000 [b]
W Ori	05:05:23.72	+01:10:39.5	−1	220 [k]	2600 [k]	3500 [k]	7.0×10^{-8} [k]	11	1500 [k]	4.3×10^{13} [k]	333 [h]
CRL 67	00:27:41.10	+69:38:51.5	−27.5	1410 [d]	2500 [n]	9817 [d]	1.1×10^{-5} [d]	16	1200 [n]	1.8×10^{14} [n]	495 [d]
CRL 190	01:17:51.62	+67:13:55.4	−39.5	2790 [d]	2500 [c]	16750 [d]	6.4×10^{-5} [d]	17	1000 [c]	4.7×10^{14} [c]	424 [d]
S Aur	05:27:07.45	+34:08:58.6	−17	300 [k]	3000 [k]	8900 [k]	4.0×10^{-7} [k]	24.5	1500 [k]	7.3×10^{13} [k]	500 [h]
V Aql	19:04:24.15	−05:41:05.4	+53.5	330 [k]	2800 [k]	6500 [k]	1.4×10^{-7} [k]	8	1500 [k]	6.1×10^{13} [k]	500 [h]
CRL 2513	20:09:14.25	+31:25:44.9	+17.5	1760 [d]	2500 [c]	8300 [c]	2.0×10^{-5} [d]	25.5	1200 [c]	1.6×10^{14} [c]	453 [d]
CRL 2477	19:56:48.43	+30:43:59.9	+5	3380 [m]	3000 [m]	13200 [m]	1.1×10^{-4} [m]	20	1800 [m]	2.8×10^{14} [m]	532 [d]
CRL 2494	20:01:08.51	+40:55:40.2	+29	1480 [b]	2400 [b]	10200 [b]	7.5×10^{-6} [b]	20	1200 [n]	2.3×10^{14} [b]	436 [d]
RV Aqr	21:05:51.74	−00:12:42.0	+0.5	670 [k]	2200 [k]	6800 [k]	2.3×10^{-6} [b]	15	1300 [k]	7.6×10^{13} [k]	200 [h]
ST Cam	04:51:13.35	+68:10:07.6	−13.6	360 [k]	2800 [k]	4400 [k]	1.3×10^{-7} [k]	8.9	1500 [k]	5.0×10^{13} [k]	500 [h]

References. [a] Agúndez et al. (2012), [b] Danilovich et al. (2015), [c] Groenewegen et al. (1998), [d] Groenewegen et al. (2002), [e] Guandalini & Cristallo (2013), [f] Guandalini et al. (2006), [g] Ramstedt et al. (2014), [h] Schöier & Olofsson et al. (2001), [i] parameters of the present-day wind of U Cam from Schöier et al. (2005), [j] Schöier et al. (2006), [k] Schöier et al. (2013), [m] Speck et al. (2009), [n] assumed value for the stellar effective temperature $T_\star$ is 2500 K, for the condensation radius r_c is 5 $R_\star$, for the dust temperature at the condensation radius $T_d(r_c)$ is 1200 K, and for the gas-to-dust mass ratio Ψ is 300.

molecule have been reported in only a few other C-rich AGB or post-AGB objects: IRAS 15194−5115 (Nyman et al. 1993), CRL 2688 (Bachiller et al. 1997), CIT 6 (Zhang et al. 2009a), and CRL 3068 (Zhang et al. 2009b). The diatomic molecule SiC was found by Cernicharo et al. (1989) in IRC +10216, and more recently Cernicharo et al. (2015b) have reported on the discovery of Si_2C toward the same source. IRC +10216 is the only source where SiC_2 has been thoroughly studied across the mm and sub-mm ranges (Lucas et al. 1995; Cernicharo et al. 2010; Patel et al. 2011; Müller et al. 2012; Fonfría et al. 2014; Velilla Prieto et al. 2015) and where SiC and Si_2C detections have been reported. The scenario emerged from the studies of IRC +10216 is that only SiC_2 and Si_2C are present in the innermost regions, while SiC is probably a photodissociation product of these two triatomic molecules and it is thus present in the outer envelope. The U-shaped line profiles of SiC (Cernicharo et al. 2000) and the upper limits derived to its abundance in the inner envelope (Velilla Prieto et al. 2015) support this idea. Moreover, chemical equilibrium calculations predict abundant SiC_2 and Si_2C but little SiC in the hot and dense surroundings of the AGB star (Tejero & Cernicharo 1991; Yasuda & Kozasa 2012; Cernicharo et al. 2015b). It therefore seems that the gas-phase molecule SiC is not an important building block of SiC dust, while SiC_2 and Si_2C are probably the main gas-phase precursors. In addition to these species, other molecules containing an Si−C bond detected in IRC +10216 are SiC_3 (Apponi et al. 1999), SiC_4 (Ohishi et al. 1989), SiCN (Guélin et al. 2000), SiH_3CN, and CH_3SiH_3 (Agúndez et al. 2014; Cernicharo et al. 2017), but their abundances are low and the observed line profiles suggest that they are formed in the external layers of the envelope.

Most of our knowledge about the role of the SiC_2, SiC, and Si_2C molecules as gas-phase precursors of silicon carbide dust comes from the study of IRC +10216, but little is known about how widespread these molecules are in other carbon stars, what their relative abundances are, and what their role in the formation of SiC dust is. Here we present the results of a systematic survey carried out with the IRAM 30 m telescope to observe these three molecules in a sample of 25 C-rich AGB stars. We report the detection of SiC_2 in most of the sources and of the radical SiC in about half of them. The sample of stars and observational details are presented in Sect. 2 and the main results obtained from the observations in Sect. 3. In Sect. 4 we describe the model and the excitation and radiative transfer calculations, and discuss the results from these calculations in Sect. 5. Finally, we discuss the implications of the derived SiC_2 abundances in Sect. 6, and present our conclusions in Sect. 7.

2. Observations

The observations were carried out in February and May 2016 with the IRAM 30 m telescope, located at Pico Veleta (Spain). We selected a sample of 25 C-rich AGB stars with intense molecular emission, mainly based on the intensity of the HCN J = 1−0 line (Loup et al. 1993; Bujarrabal et al. 1994; Schöier et al. 2013). The list of sources and their parameters are given in Table 1. The coordinates and LSR systemic velocities were taken from the literature (Olofsson et al. 1993; Groenewegen et al. 1996, 2002; Cernicharo et al. 2000; Sánchez Contreras & Sahai 2012) and checked using the SIMBAD astronomical database[1]

[1] http://simbad.u-strasbg.fr/Simbad

(Wenger et al. 2000). For some sources, systemic velocities were not accurately known and thus we determined them from intense lines observed in this study (see below).

We used the E150 receiver in dual side band, with image rejections >10 dB, and observed the frequency ranges 138.5−146.3 GHz and 154.1−161.9 GHz (in the lower and upper side bands, respectively). This spectral setup was chosen to include several strong lines of SiC_2, various lines of Si_2C, and the $J = 4-3$ rotational transition of the radical SiC in its $^3\Pi_2$ state. The strongest lines of these three species covered in the observed frequency range are listed in Table 2. In the IRC +10216 spectrum, the line intensity ratios of the three species are typically SiC_2:Si_2C:SiC ∼ 100:1:10 (Cernicharo et al. 2000, 2015b), and thus we expect that in the rest of the sources of the sample, SiC_2 will be the most easily detectable molecule, while Si_2C will display the weakest lines and thus will be the most difficult to detect. The adopted spectral range also covers lines which are typically intense in carbon-rich circumstellar envelopes, such as HC_3N $J = 16-15$ and $J = 17-16$, C_4H $N = 15-14$ and $N = 17-16$, and SiS $J = 8-7$.

The beam size of the telescope at these frequencies is in the range 15.0−17.5″. We used the wobbler-switching technique, with the secondary mirror nutating by 3′ at a rate of 0.5 Hz. The focus was regularly checked on Venus and Uranus and the pointing of the telescope was systematically checked on a nearby quasar before observing each AGB star. The error in the pointing is estimated to be 2−3″. The E150 receiver was connected to a fast Fourier transform spectrometer providing a spectral resolution of 200 kHz. The weather was good and stable during most of the observations, with typical amounts of precipitable water vapor of 1−3 mm and system temperatures ranging from 80 K to 150 K. The intensity scale, calibrated using two absorbers at different temperatures and the atmospheric transmission model (ATM; Cernicharo 1985; Pardo et al. 2001), is expressed in terms of T_A^*, the antenna temperature corrected for atmospheric absorption and for antenna ohmic and spillover losses. To convert to main beam antenna temperature, T_A^* has to be divided by 0.78 (the ratio of the main beam efficiency to the forward efficiency of the IRAM 30 m telescope at the observed frequencies[2]). The error in the intensities due to calibration is estimated to be ∼20%.

The data were reduced using the software CLASS within the package GILDAS[3]. For each source, we averaged the spectra corresponding to the horizontal and vertical polarizations, subtracted a baseline consisting of a first-order polynomial, and smoothed the resulting spectrum to a spectral resolution of 1 MHz, which is good enough to spectrally resolve the lines whose widths in most sources are typically in the range 15−50 km s^{-1} (7.5−25 MHz at the observed frequencies). Typical on-source integration times, after averaging horizontal and vertical polarizations, were ∼1 h for each source, resulting in T_A^* rms noise levels per 1 MHz channel of 2−5 mK.

3. Results from observations

The observations resulted in the detection of SiC_2 in 22 out of the 25 targeted sources, i.e., all sources except UU Aur, R Lep, and ST Cam. The five rotational transitions of SiC_2 listed in Table 2, which have upper level energies in the range 31−55 K, were clearly detected in most of the 22 sources where

[2] http://www.iram.es/IRAMES/mainWiki/Iram30mEfficiencies

[3] http://www.iram.fr/IRAMFR/GILDAS

Table 2. Covered rotational transitions of SiC_2, Si_2C, and SiC.

Transition	Frequency (MHz)	A_{ul} (s^{-1})	E_u (K)
	SiC_2		
$6_{2,5}-5_{2,4}$	140920.171	7.65×10^{-5}	31.5
$6_{4,3}-5_{4,2}$	141751.492	4.87×10^{-5}	55.0
$6_{4,2}-5_{4,1}$	141755.360	4.87×10^{-5}	55.0
$6_{2,4}-5_{2,3}$	145325.875	8.39×10^{-5}	32.0
$7_{0,7}-6_{0,6}$	158499.228	1.23×10^{-4}	31.0
	Si_2C		
$11_{1,11}-10_{0,10}$	144033.475	9.57×10^{-6}	29.3
$22_{2,20}-22_{1,21}$	155600.100	1.54×10^{-5}	115.0
$13_{1,13}-12_{0,12}$	157768.156	1.28×10^{-5}	39.3
$20_{2,18}-20_{1,19}$	157959.754	1.54×10^{-5}	97.4
$18_{2,16}-18_{1,17}$	160644.790	1.55×10^{-5}	81.4
	SiC		
$^3\Pi_2$ $J = 4-3$	157494.101	3.98×10^{-5}	13.2

SiC_2 was identified. The lines corresponding to the rotational transitions $6_{4,3}-5_{4,2}$ and $6_{4,2}-5_{4,1}$ appear blended together because line widths are larger than the frequency separation of the two transitions, although in most sources each of these lines could be fitted individually. The observed line profiles of SiC_2 are shown in Fig. 1 and the parameters derived from line fits using the `shell` method of CLASS[3] are given in Table A.1. We note that in U Cam, the line profiles of SiC_2 are consistent with emission arising exclusively from the present-day wind, rather than from the detached envelope (compare line profiles in Fig. 1 with those of CO in Schöier et al. 2005).

We also report the detection of SiC in 12 of the 25 targeted C-rich AGB envelopes (see Fig. 2). We note that prior to this study, this radical had been detected only in the C-star envelope IRC +10216 (Cernicharo et al. 1989). The SiC emission line is relatively strong in IRC +10216, CIT 6, CRL 3068, and LP And, while it is marginally detected in IRC +30374, V Cyg, V384 Per, IRC +60144, IRC +20370, CRL 67, CRL 2477, and CRL 2494. In Fig. 3 we compare the velocity-integrated intensity of the SiC $^3\Pi_2$ $J = 4-3$ line with that of the SiC_2 $7_{0,7}-6_{0,6}$ line. We note that the SiC lines are brighter in the sources where SiC_2 is more intense, which suggests that the abundances of both species are correlated, as is expected if the radical SiC is a photodissociation product of SiC_2. This suggests that the nondetection of SiC in some of the sources is probably due to a lack of sensitivity and not due to a low fractional abundance of the radical. The related molecule Si_2C was not detected in any of the targeted sources, with the exception of IRC +10216, which at present is the only source in which this molecule has been identified (Cernicharo et al. 2015b). In IRC +10216, the lines of Si_2C are typically 100 times less intense than those of SiC_2. This difference in intensity is not due to a significant difference in abundance, but it is related to the larger partition function of Si_2C and its lower dipole moment, as discussed in detail by Cernicharo et al. (2015b). If the same relative intensities between SiC_2 and Si_2C holds for the rest of C-star envelopes, the nondetection of disilicon carbide is very likely due to an insufficient sensitivity.

In addition to the lines of SiC_2 and SiC, we also detected within the frequency range covered 138.5−146.3 GHz and 154.1−161.9 GHz, emission lines of other species typically present in the spectra of carbon-rich AGB envelopes. For example, the $J = 16-15$ and $J = 17-16$ lines of HC_3N and the

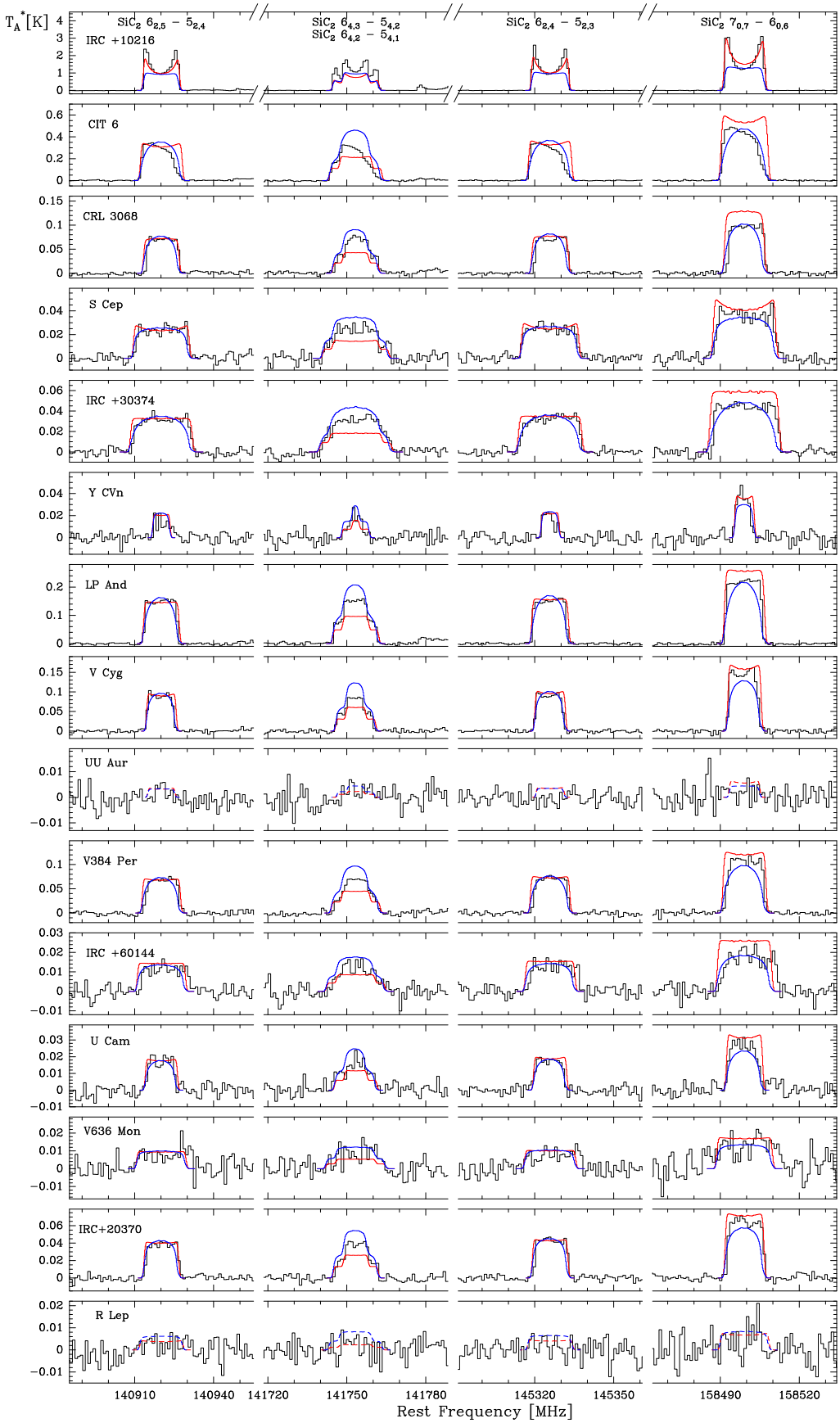

Fig. 1. Rotational lines of SiC_2 observed with the IRAM 30 m telescope in the 25 target sources (black histograms). The spectral resolution of the observed lines is 1 MHz. The blue lines are the calculated emerging line profiles from the best-fit model using the LVG method. The red lines are the predicted line profiles assuming LTE excitation. Dashed lines correspond to calculated lines profiles for those sources where SiC_2 was not detected.

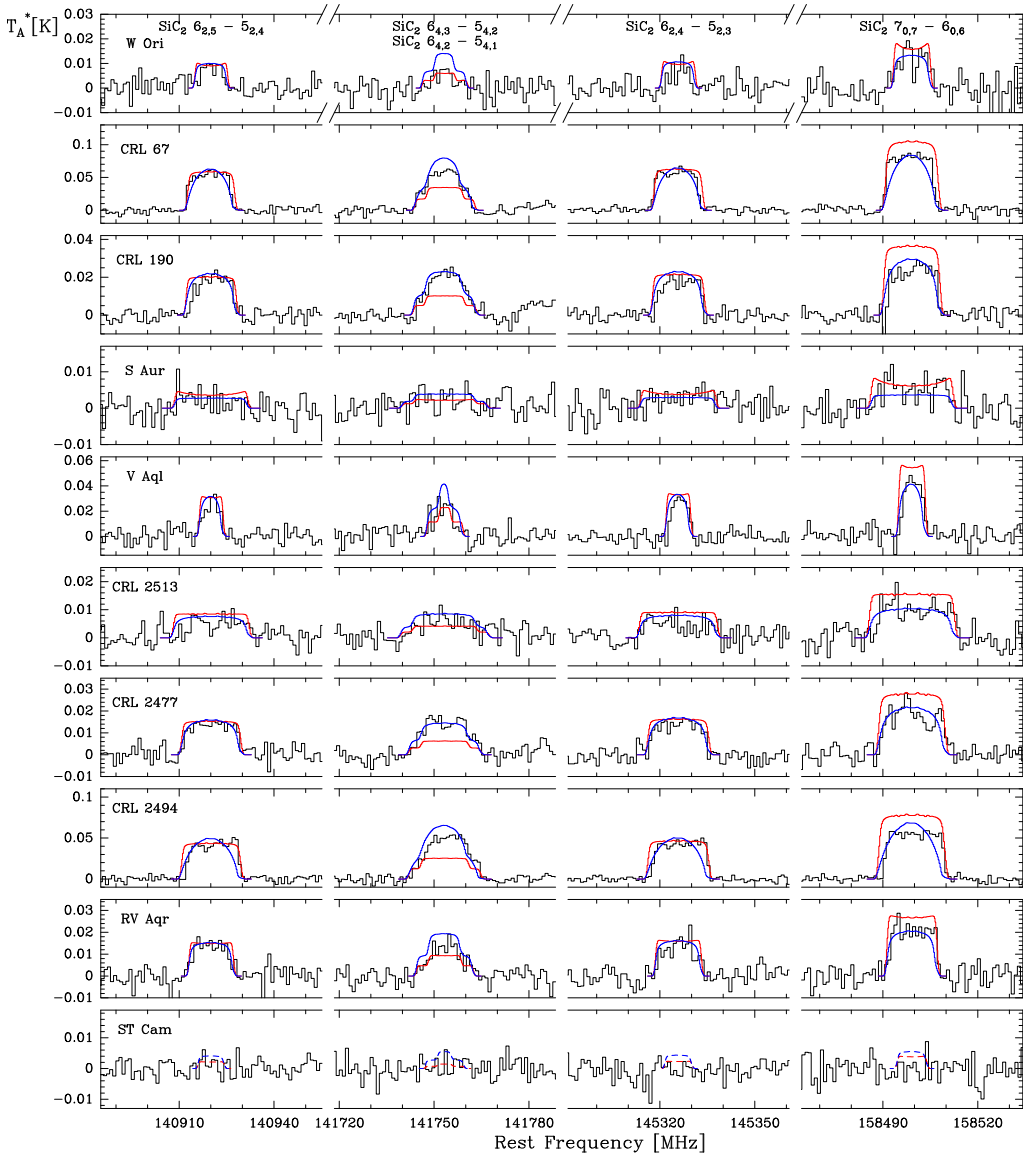

Fig. 1. continued.

$J = 3-2$ line of some isotopologues of carbon monosulfide, mainly $C^{34}S$ and ^{13}CS, are intense and prevalent among most of the sources. The $J = 8-7$ line of SiS is observed in many of the envelopes as one of the most intense lines, but it is not even detected in some of the other sources. The $N = 15-14$ and $N = 17-16$ lines of C_4H and the $N = 14-13$ and $N = 16-15$ of C_3N are also intense in some of the envelopes, although in many of them the lines of these two radicals are below the detection limit. In those sources where molecular emission is most intense, such as CIT 6, CRL 3068, and LP And, lines of other molecules such as l-C_3H, c-C_3H_2, C_2S, HC_5N, and rare isotopologues of CS, SiS, SiC_2, and HC_3N are detected. In a couple of sources, UU Aur and ST Cam, no molecular emission was observed above a detection threshold of a few mK in the covered frequency range.

The availability of strong lines of molecules such as HC_3N, SiS, C_4H, $C^{34}S$, and SiC_2 in our data allows us to derive accurate values of the velocity of the source V_{LSR} and of the terminal expansion velocity of the envelope V_{exp} in most of the sources. These two parameters are reported in the literature mainly from CO $J = 1-0$ and $J = 2-1$ lines (Loup et al. 1993; Olofsson et al. 1993; Groenewegen et al. 1996, 2002 with varying degrees of accuracy. We carried out a critical evaluation of the values of V_{LSR} and V_{exp} derived from our data and those in the literature. In cases where our lines have a well-defined shape, the values from our dataset were preferred, whereas when lines show a less clear shape, the values from literature were favored. The final values of V_{LSR} and V_{exp} adopted in this work are given in Table 1.

In this article we focus on the analysis of SiC_2 and leave the interpretation of other molecules for future studies. Silicon dicarbide was detected in most of the targeted sources and we aim to model its emission and determine its abundance in each source to provide a global view of how abundant this molecule is in circumstellar envelopes around C-rich AGB stars.

4. SiC_2 radiative transfer modeling

4.1. Envelope model

We adopted a common physical scenario to model all sources consisting of a spherically symmetric envelope of gas and dust expanding with a constant velocity and mass-loss rate around

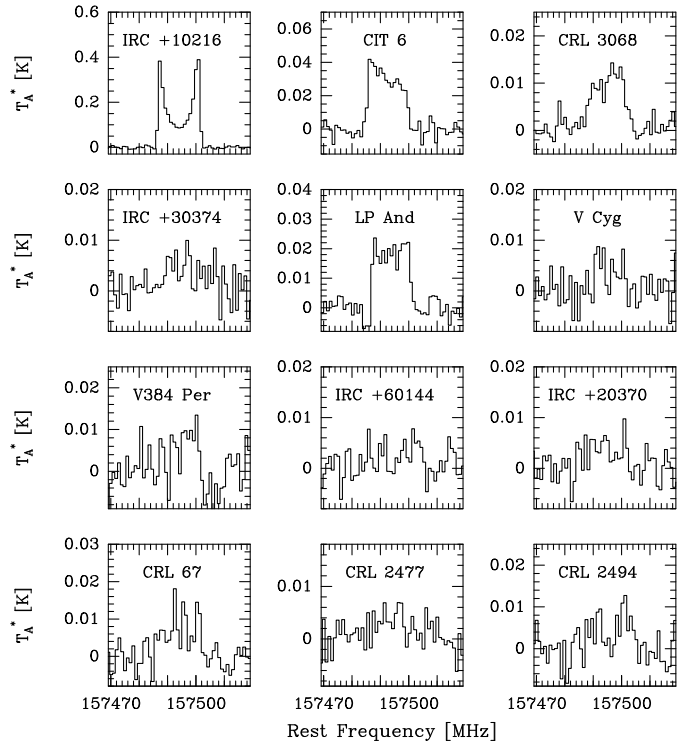

Fig. 2. SiC $^3\Pi_2$ $J = 4-3$ line observed in 12 out of the 25 sources in our sample. The spectral resolution is 1 MHz.

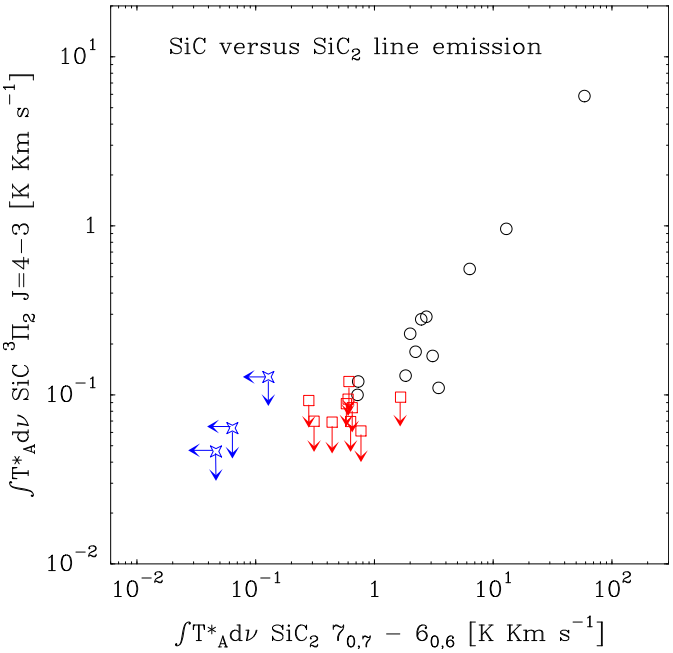

Fig. 3. Velocity-integrated intensity of the SiC $^3\Pi_2$ $J = 4-3$ line vs. the velocity-integrated intensity of the SiC_2 $7_{0,7}-6_{0,6}$ line. Black circles correspond to sources where both SiC_2 and SiC are detected, red squares to envelopes where SiC_2 is detected but not SiC, and blue stars to sources where neither SiC nor SiC_2 is detected.

a central AGB star. The parameters of the star and envelope adopted for the different sources are detailed in Table 1.

The central AGB star is characterized by an effective temperature T_* and a luminosity L_*. The stellar radius R_* is then determined by T_* and L_* using the Stefan-Boltzmann law. Effective temperatures for the photosphere of AGB stars, typically in the range 2000−3000 K, are difficult to estimate accurately. For most of the stars in our sample, we adopted the values of T_* from studies where T_* is derived by modeling the spectral energy distribution (SED) of each star (Schöier et al. 2005, 2013; Agúndez et al. 2012; Ramstedt & Olofsson 2014; Danilovich et al. 2015). In some cases, the adopted values of T_* are taken from studies where the effective temperature was chosen to be a round number that fitted the SED reasonably well (Groenewegen et al. 1998; Speck et al. 2009). For those objects for which T_* was not available from the literature, we assumed a typical value for AGB stars of 2500 K. Regarding the stellar luminosities L_*, we adopted values from the literature (see references in Table 1) in which they were mostly derived using the period-luminosity relation for Mira variables.

The spherical envelope is described by the radial profile of various physical quantities, such as the gas density, the temperature of gas and dust, the expansion velocity, and the microturbulence velocity. The gas density as a function of the distance r from the star is determined by the law of conservation of mass as

$$n_{\rm g} = \frac{\dot{M}}{\overline{m}_{\rm g}\, 4\pi\, r^2\, V_{\rm e}}, \tag{1}$$

where $n_{\rm g}$ is the number of gas particles per unit volume, $\overline{m}_{\rm g}$ is the average mass of gas particles, $\dot{M}$ is the mass-loss rate, and $V_{\rm e}$ is the expansion velocity of the envelope. We assume that $V_{\rm e}$ is equal to the terminal expansion velocity of the envelope $V_{\rm exp}$ across the entire envelope. This is certainly not true inside the acceleration region, but these inner layers contribute little to the emission of the SiC_2 lines observed here. We adopt $\overline{m}_{\rm g} = 2.3$ amu, adequate for a gas composed mainly of H_2, He with a solar elemental abundance, and CO with an abundance of $\sim 10^{-3}$ relative to H_2. Mass-loss rates were taken from the literature where $\dot{M}$ was determined by modeling observations of multiple CO lines (see references in Table 1).

The radial structure of the gas kinetic temperature $T_{\rm k}$ is described by a power law of the type

$$T_{\rm k} = T_\star \left(\frac{r}{R_\star}\right)^{-\delta}, \tag{2}$$

where R_* is the stellar radius. In reality, the gas kinetic temperature is determined by a balance between the different heating and cooling processes at work, and cannot be accurately described by a single power law across the entire envelope. We do not aim to derive the gas kinetic temperature radial profile for each individual source, and thus for simplicity we adopt a uniform value of $\delta = 0.7$, which is in line with findings from previous studies of circumstellar envelopes around AGB stars (e.g., Schöier & Olofsson 2001; De Beck et al. 2010; Guélin et al. 2018).

The microturbulence velocity is assumed to be $1\,{\rm km\,s^{-1}}$ throughout the envelope, which is within the range of values 0.65–1.5 $\rm km\,s^{-1}$, derived in the literature for the C-rich envelope IRC +10216 (Skinner et al. 1999; De Beck et al. 2012); however, this parameter has a limited impact when modeling the SiC_2 lines because it is well below the terminal expansion velocity of the wind for all sources.

We also consider the dusty component of the envelope, although, as will be discussed below, in our models dust plays a minor role in the excitation of the rotational lines of SiC_2 observed. We consider spherical grains of amorphous carbon with a radius of 0.1 μm, a mass density of 2 g $\rm cm^{-3}$, and optical properties from Suh (2000). Dust grains are assumed to be

present from the dust condensation radius r_c with a constant gas-to-dust mass ratio Ψ. The radial structure of the dust temperature T_d is assumed to be given by the power-law expression

$$T_d = T_d(r_c)\left(\frac{r}{r_c}\right)^{-\delta_d}, \quad (3)$$

where we assume $\delta_d = 0.4$ based on theoretical expectations for carbonaceous grains (e.g., Kerschbaum et al. 2007). This value is also close to that derived for IRC +10216 (Agúndez et al. 2012). The values of Ψ, r_c, $T_d(r_c)$ were taken from the literature where they are typically derived by modeling the SED using photometric data, such as IRAS and 2MASS fluxes and in some cases submillimeter data (Schöier et al. 2006, 2013; Ramstedt & Olofsson 2014; Danilovich et al. 2015). In cases where those parameters were not available in the literature, we assumed a typical value of 5 $R_\star$ for r_c, 1200 K for $T_d(r_c)$, and 300 for the gas-to-dust mass ratio Ψ.

The adopted distances to the AGB stars were taken from the literature (see references in Table 1). The data include measurements from HIPPARCOS parallaxes and estimations based on bolometric magnitudes using the period-luminosity relation for Mira variables. When nothing else was available, the distances were estimated assuming $L_* = 10^4\ L_\odot$.

4.2. Excitation and radiative transfer calculations

We performed excitation and radiative transfer calculations to model the line emission of SiC_2 based on the multi-shell large velocity gradient (LVG) method. The circumstellar envelope is divided into a number of concentric shells, each of which has a characteristic set of physical properties and SiC_2 abundance, and statistical equilibrium equations are solved in each of them. In each shell, the contribution of the background radiation field (cosmic microwave background, stellar radiation, and thermal emission from surrounding dust) is included (see Agúndez et al. 2012, for further details). For the current study, the LVG method provides a good compromise between the assumption of local thermal equilibrium (LTE) and more computationally expensive nonlocal methods. Rate coefficients for the rotational excitation of SiC_2 through collisions have been computed theoretically (Chandra & Kegel 2000), which makes it worth using more advanced methods than LTE. Our calculations indicate that the emission from the SiC_2 lines observed here arises from intermediate regions in the envelope where the rotational levels are not fully thermalized (see Sect. 5). Moreover, the observed lines of SiC_2 are optically thin in most sources, which implies that the LVG method should be accurate enough.

In the excitation calculations, we consider rotational levels up to $J = 39$ and $K_a = 20$ within the ground vibrational state of SiC_2 (i.e., a total number of 620 energy levels). Level energies and transition frequencies were calculated from the rotational constants reported by Müller et al. (2012), and line strengths for rotational transitions were computed from the dipole moment, 2.393 ± 0.006 D, measured by Suenram et al. (1989). The rate coefficients for excitation through inelastic collisions with H_2 and He were taken from Chandra & Kegel (2000), who calculated rate coefficients for transitions between the first 40 rotational levels in the temperature range 25−125 K. At temperatures higher than 125 K, we adopted the theoretical rate coefficients calculated at 125 K and did not perform an extrapolation in temperature. This could introduce uncertainties in the excitation calculations. To evaluate the impact of this assumption, we carried out calculations in which we implemented a linear extrapolation in temperature of the rate coefficients at $T_k > 125$ K and verified that the calculated line profiles of the SiC_2 transitions observed were not sensitive to the particular choice of the collision rate coefficients at temperatures higher than 125 K. The reason is that, as is discussed in Sect. 5, most of the SiC_2 emission detected with the IRAM 30 m telescope arise from intermediate regions of the envelope, where gas kinetic temperatures are in the range ∼50−300 K, i.e., not excessively far from the 25−125 K temperature range. Since the calculations of Chandra & Kegel (2000) only include the first 40 rotational levels, for transitions involving higher levels, the de-excitation rate coefficients were approximated using the expression

$$\log\gamma = -10 - 0.25\,(J' - J'') - 0.45\,|K'_a - K''_a|, \quad (4)$$

where γ is the rate coefficient in units of $cm^3\ s^{-1}$, and $'$ and $''$ denote the upper and lower level, respectively. Equation (4) provides a first-order approximation for asymmetric rotors, based on theoretical calculations carried out for the molecules SiC_2 (Chandra & Kegel 2000), SO_2 (Green 1995), and HCO_2^+ (Hammami et al. 2007).

4.3. The SiC_2 radial abundance profile

We consider that SiC_2 is formed close to the star with a given fractional abundance that remains constant throughout the envelope up to the outer regions of the envelope, where it is photodissociated by the ambient ultraviolet radiation field of the local interstellar medium. To compute the falloff of abundance due to photodissociation, we assume that the photodissociation rate of SiC_2 is given by the expression $\alpha\exp(-\beta A_V)$, where A_V is the visual extinction. We adopt an unattenuated rate of $\alpha = 10^{-10}\ s^{-1}$ and a dust shielding factor of $\beta = 1.7$, values which are merely educated guesses (MacKay & Charnley 1999) because the photodissociation cross section of SiC_2 is not well known. The radial variation of the SiC_2 abundance in the expanding envelope is then given by the differential equation (Jura & Morris 1981; Huggins & Glassgold 1982)

$$\frac{df}{dr} = -\frac{\alpha}{V_{exp}}\exp\left[-\left(\frac{r_d}{r}\right)\right] f, \quad (5)$$

where f is the fractional abundance of SiC_2 relative to H_2 and r_d is a parameter that can be considered as a photodissociation radius and which is given by

$$r_d = \frac{\beta\,\dot{M}}{4\pi\,V_{exp}\,\overline{m}_g\,1.87\times10^{21}}, \quad (6)$$

where the numerical value is the canonical N_H/A_V ratio given by Bohlin et al. (1978) for the local interstellar medium. The solution to Eq. (5) can be expressed as

$$\ln\frac{f}{f_0} = -\frac{\alpha}{V_{exp}}\left\{\left[r_d\,E_i\left(-\frac{r_d}{r}\right) + r\,e^{(-r_d/r)}\right] - \left[r_d\,E_i\left(-\frac{r_d}{R_*}\right) + R_*\,e^{(-r_d/R_*)}\right]\right\}, \quad (7)$$

where E_i is the exponential integral. This approach provides a simple and accurate way to take into account the abundance falloff due to photodissociation. Once the physical structure of the envelope is set and a given initial abundance f_0 is chosen, the abundance profile $f(r)$ becomes fully described by Eq. (7). We note that it is likely that SiC_2 can experience an abundance decline around the dust formation zone. The adopted abundance

profile, however, does not include such a feature since we are tracing a specific region of the envelope, more specifically the intermediate one (see Sect. 5), and thus it is not possible to accurately derive the radial abundance profile from the very inner regions out to the outer envelope. In this work we thus determine the mean abundance of SiC_2 in the intermediate regions of the envelope of the studied sources.

In summary, to model the emission lines of SiC_2 and determine its abundance in the observed sources we constructed a model of the envelope for each source, as described in Sect. 4.1, with the parameters given in Table 1. We then performed excitation and radiative transfer calculations, as explained in Sect. 4.2, using the abundance profile described in Sect. 4.3. We varied the initial fractional abundance of SiC_2 relative to H_2, f_0 in Eq. (7), until the calculated line profiles matched the observed ones. We choose as the best-fit model the one that results in the best overall agreement between calculated and observed line profiles for the entire set of SiC_2 lines observed. In those cases where no lines of SiC_2 are detected, we derive upper limits to the abundance of SiC_2 by choosing the maximum abundance that results in line intensities compatible with the noise level of the observations.

5. Results from SiC_2 radiative transfer modeling

In most sources (see Fig. 1), the shapes of the SiC_2 lines observed are nearly flat-topped, which is indicative of optically thin emission not resolved by the 15.0−17.5″ beam of the IRAM 30 m telescope. One notable exception is IRC +10216, whose close proximity (130 pc) means that the emission is spatially resolved by the telescope beam, and the line profiles show a marked double-peaked character. The calculated line profiles resulting from our best-fit LVG model for each of the sources are shown in blue in Fig. 1, where they are compared with the observed line profiles. The agreement between calculated and observed line shapes is good in most sources, except in IRC +10216, for which the LVG model produces a less marked U-shape than observed, and a few sources like LP And, for which the calculated lines are more curved than flat-topped; in other words, in some sources the LVG model seems to result in lines that are more optically thick than indicated by the observed line shapes. To investigate this, we also ran models where we assumed LTE excitation for SiC_2. These models tend to produce line shapes that are in better agreement with the observed ones in sources like IRC +10216, where calculated line profiles have a clearer U-shaped character, and LP And, where line shapes are more flat-topped (see red lines in Fig. 1). This suggests that the LVG model lacks sufficient excitation for the levels involved in the observed SiC_2 transitions. There are various possible causes of the suspected lack of excitation, which we discuss below.

According to the LVG model, the excitation of the rotational levels of SiC_2 in the envelopes studied is dominated by inelastic collisions with H_2 and He. Even though thermal emission from dust is included in the model, it has little impact on the excitation of the observed SiC_2 rotational lines. The five lines of SiC_2 observed here involve upper levels with relatively low energies (31−55 K), and thus are preferentially excited in intermediate layers of the envelope where gas kinetic temperatures are of this order. In Fig. 4 we show the contribution to the velocity-integrated intensity of the five SiC_2 lines observed as a function of the impact parameter relative to the position of the star for two sources in our sample, U Cam and IRC +30374. These two envelopes are representative of very different mass-loss rates. While U Cam lies in the lower range, with $\dot{M} = 2\times10^{-7}\ M_\odot\ \mathrm{yr}^{-1}$, IRC +30374 lies at the higher end, with $\dot{M} = 10^{-5}\ M_\odot\ \mathrm{yr}^{-1}$. In

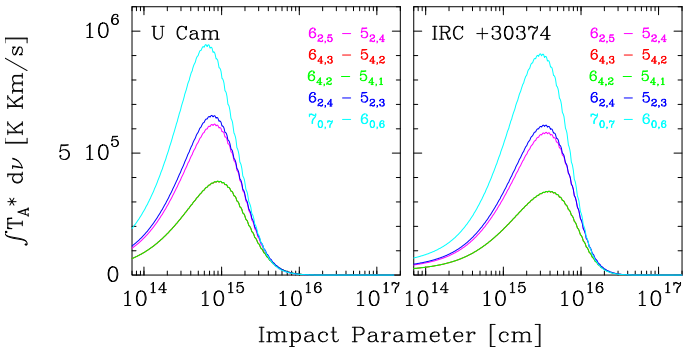

Fig. 4. Velocity-integrated intensity plotted as a function of impact parameter for the five observed SiC_2 lines in U Cam and IRC +30374. The transitions $6_{4,3}-5_{4,2}$ and $6_{4,2}-5_{4,1}$ have overlapping curves. For visualization reasons, the intensities of U Cam are multipled by a factor of 2.75.

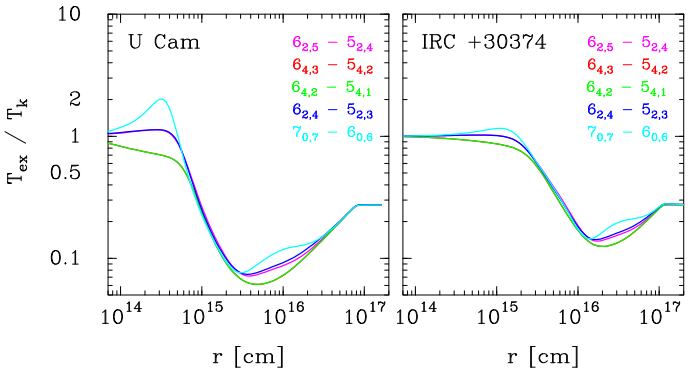

Fig. 5. Calculated ratio of excitation temperature to kinetic temperature (T_{ex}/T_k) as a function of radius for the five observed rotational transitions of SiC_2 in U Cam and IRC +30374. The transitions $6_{4,3}-5_{4,2}$ and $6_{4,2}-5_{4,1}$ have overlapping curves.

U Cam, the maximum contribution to the line emission comes from regions at $\sim10^{15}$ cm, while in the case of IRC +30374 the regions around $\sim10^{16}$ cm contribute the most to the observed emission; i.e., in envelopes with low mass-loss rates the SiC_2 rotational levels involved in the five observed transitions are only efficiently excited by collisions in the inner regions (and thus most of the emission detected in these lines comes from such regions), while in envelopes with high mass-loss rates the densities are still high enough in the outer regions to excite the SiC_2 rotational levels and thus most emission comes from these outer regions. Among the studied sources, the LVG models indicate that emission from the five SiC_2 observed lines arises typically from intermediate regions of the envelope, at radial distances in the range $10^{15}-10^{16}$ cm.

It is interesting to have a look at the excitation of SiC_2 predicted by the LVG model in the studied envelopes, in particular to the extent to which the rotational levels involved in the five observed transitions are close to or far from thermalization. In Fig. 5 we show the calculated ratio of excitation to gas kinetic temperature (T_{ex}/T_k) for the five SiC_2 transitions as a function of radius for the envelopes U Cam and IRC +30374, which lie at low and high ranges, respectively, of mass-loss rates. We see that for most transitions $T_{ex}/T_k = 1$, i.e., rotational levels are thermalized, in the hot and dense inner regions, and that as the radius increases and the gas density decreases, the rotational levels become increasingly subthermally excited, as indicated by the fact that the ratio T_{ex}/T_k falls below unity. The much lower mass-loss rate of U Cam compared to IRC +30374 implies substantially

lower densities in the envelope and thus in U Cam rotational populations start to deviate from thermalization at shorter radii than in IRC +30374. We note that in the intermediate region of the envelope from where most emission comes from, $\sim 10^{15}$ cm in U Cam and $\sim 10^{16}$ cm in IRC +30374 (see Fig. 4), the SiC_2 rotational levels are mostly subthermally excited.

As commented above, for some of the sources, the LVG model could lack sufficient excitation for the levels involved in the observed transitions of SiC_2. One possible missing source of excitation could be related to the existence of shells with an enhanced density with respect to the surrounding media (Mauron & Huggins 2000; Cordiner & Millar 2009; Cernicharo et al. 2015a; Agúndez et al. 2017; Guélin et al. 2018). From models of IRC +10216 and LP And we notice that density enhancements above a factor of 10 are needed to start to reproduce adequately the observed line shapes. In IRC +10216, the shell-intershell density contrast is just 3 (Guélin et al. 2018). It is currently unknown whether episodic mass loss in other stars could be abrupt enough to result in shell-intershell density contrasts above 10. We also note that uncertainties in the rate coefficients of SiC_2 excitation through inelastic collisions may also be at the origin of the suspected lack of excitation of SiC_2 in IRC +10216. In this sense, it would be interesting to revisit the collisional rate coefficients calculated by Chandra & Kegel (2000). Another possible missing source of excitation in the LVG model could be infrared (IR) pumping, i.e., absorption of IR photons and pumping to excited vibrational states followed by spontaneous radiative decay to rotational levels in the ground vibrational state. This effect is not included in the model for SiC_2 (mainly because there is a complete lack of information about infrared intensities), although it is an important excitation mechanism of some molecules in IRC +10216 (e.g., Agúndez & Cernicharo 2006) where the infrared flux is large (Cernicharo et al. 1999). However, vibrationally excited SiC_2 seems to be restricted to the inner layers, as indicated by the narrow lines from the vibrational states $v_3 = 1, 2$ detected with ALMA (Cernicharo et al. 2013). Moreover, if IR pumping was playing an important role for SiC_2 we could expect to see the time variation of the line intensities found by Cernicharo et al. (2014) for other molecules, but the lines of SiC_2 show a rather constant intensity along the stellar period of CW Leo, which suggests that IR pumping is not important for this molecule (Cernicharo et al. 2014).

The differences between calculated and observed line shapes for some of the sources suggests that the LVG model may lack excitation for SiC_2, and that this could happen for other sources as well. We have thus run models assuming LTE excitation for all sources. The calculated line profiles are shown in red in Fig. 1. Assuming LTE excitation throughout the whole envelope increases the excitation to outer radii, which leads to an increase in the emission size. Therefore, in general, the line opacities and fractional abundance of SiC_2 required to reproduce the observed intensities are lower when assuming LTE than when using the LVG method. Since it is unlikely that the rotational levels of SiC_2 are populated in LTE out to the outermost low-density regions of the envelope, the abundance of SiC_2 in the envelope of the observed sources is most likely between the values given by the LVG and the LTE models, which typically differ by a factor of ~3 (see Table 3).

6. Discussion

The fractional abundances of SiC_2 derived in the 25 studied envelopes are given in Table 3. We give the abundances derived using the LVG method, while those obtained assuming LTE excitation are given in the last column. The fractional abundances obtained using the LVG method range between 3.7×10^{-7} and 3.7×10^{-5} relative to H_2. Assuming that silicon has a solar elemental abundance in AGB stars (Asplund et al. 2009), the maximum possible abundance of SiC_2 relative to H_2 is 6.5×10^{-5}. Therefore, the high fractional abundances of SiC_2 of a few times 10^{-5} derived in some of the envelopes imply that gaseous SiC_2 locks an important fraction of the available silicon, possibly making it a major reservoir of this element. We note, however, that if the abundances are closer to the values derived under LTE, the maximum abundances derived for SiC_2 are $\sim 7 \times 10^{-6}$ relative to H_2, which would imply that SiC_2 locks at most ~10% of the available silicon.

Table 3. Derived fractional abundances of SiC_2.

Name	$\dot{M}$ ($M_\odot$ yr^{-1})	V_{exp} (km s^{-1})	$f_0(SiC_2)_{LVG}$	$f_0(SiC_2)_{LTE}$
IRC +10216	2.0×10^{-5}	14.5	3.7×10^{-7}	3.7×10^{-7}
CIT 6	6.0×10^{-6}	17	1.1×10^{-5}	3.4×10^{-6}
CRL 3068	2.5×10^{-5}	14.5	1.9×10^{-6}	7.2×10^{-7}
S Cep	1.2×10^{-6}	22.5	1.0×10^{-5}	2.0×10^{-6}
IRC +30374	1.0×10^{-5}	25	9.7×10^{-6}	2.3×10^{-6}
Y CVn	1.5×10^{-7}	7	4.0×10^{-6}	1.7×10^{-6}
LP And	7.0×10^{-6}	14.5	6.8×10^{-6}	2.2×10^{-6}
V Cyg	1.6×10^{-6}	12	6.6×10^{-6}	2.3×10^{-6}
UU Aur	2.4×10^{-7}	10.6	$<1.0 \times 10^{-6}$	$<3.5 \times 10^{-7}$
V384 Per	2.3×10^{-6}	15.5	1.3×10^{-5}	3.6×10^{-6}
IRC +60144	3.7×10^{-6}	19.5	6.0×10^{-6}	1.8×10^{-6}
U Cam	2.0×10^{-7}	13	3.7×10^{-5}	6.7×10^{-6}
V636 Mon	5.8×10^{-6}	20	1.7×10^{-6}	5.1×10^{-7}
IRC +20370	3.0×10^{-6}	14	4.2×10^{-6}	1.5×10^{-6}
R Lep	8.7×10^{-7}	17.5	$<2.7 \times 10^{-6}$	$<4.1 \times 10^{-7}$
W Ori	7.0×10^{-8}	11	1.4×10^{-5}	2.4×10^{-6}
CRL 67	1.1×10^{-5}	16	1.0×10^{-5}	2.6×10^{-6}
CRL 190	6.4×10^{-5}	17	8.8×10^{-7}	2.9×10^{-7}
S Aur	4.0×10^{-7}	24.5	3.6×10^{-6}	7.3×10^{-7}
V Aql	1.4×10^{-7}	8	2.0×10^{-5}	7.3×10^{-6}
CRL 2513	2.0×10^{-5}	25.5	1.6×10^{-6}	5.3×10^{-7}
CRL 2477	1.1×10^{-4}	20	6.0×10^{-7}	1.9×10^{-7}
CRL 2494	7.5×10^{-6}	20	2.7×10^{-5}	4.9×10^{-6}
RV Aqr	2.3×10^{-6}	15	3.0×10^{-6}	1.0×10^{-6}
ST Cam	1.3×10^{-7}	8.9	$<4.0 \times 10^{-6}$	$<6.0 \times 10^{-7}$

In most of the carbon-rich AGB envelopes in our sample, SiC_2 abundances are reported for the first time in this work. The only source where SiC_2 has been previously studied in detail is IRC +10216, which in fact has the lowest fractional abundance of SiC_2 among all the sources in our sample (3.7×10^{-7} relative to H_2, see Table 3). Cernicharo et al. (2010) observed 55 rotational transitions of SiC_2 in IRC +10216 using the HIFI spectrometer on board *Herschel*. These authors derive an abundance of 2×10^{-7} relative to H_2 in the inner regions of the envelope using an LTE radiative transfer analysis. Based on mm-wave interferometric observations, Lucas et al. (1995) derive an abundance relative to H_2 of 5×10^{-7} for the inner regions, and more recently Fonfría et al. (2014) inferred an abundance relative to H_2 of 8×10^{-7} at the stellar surface decreasing down to 8×10^{-8} at 20 R_*. The SiC_2 abundance derived in this work for IRC +10216 (3.7×10^{-7}) is in good agreement with the values reported in these articles.

The fractional abundance of SiC_2 shows an interesting trend with either the mass-loss rate $\dot{M}$ or the density in the envelope, evaluated through the quantity $\dot{M}/V_{exp}$. As shown in Fig. 6, SiC_2

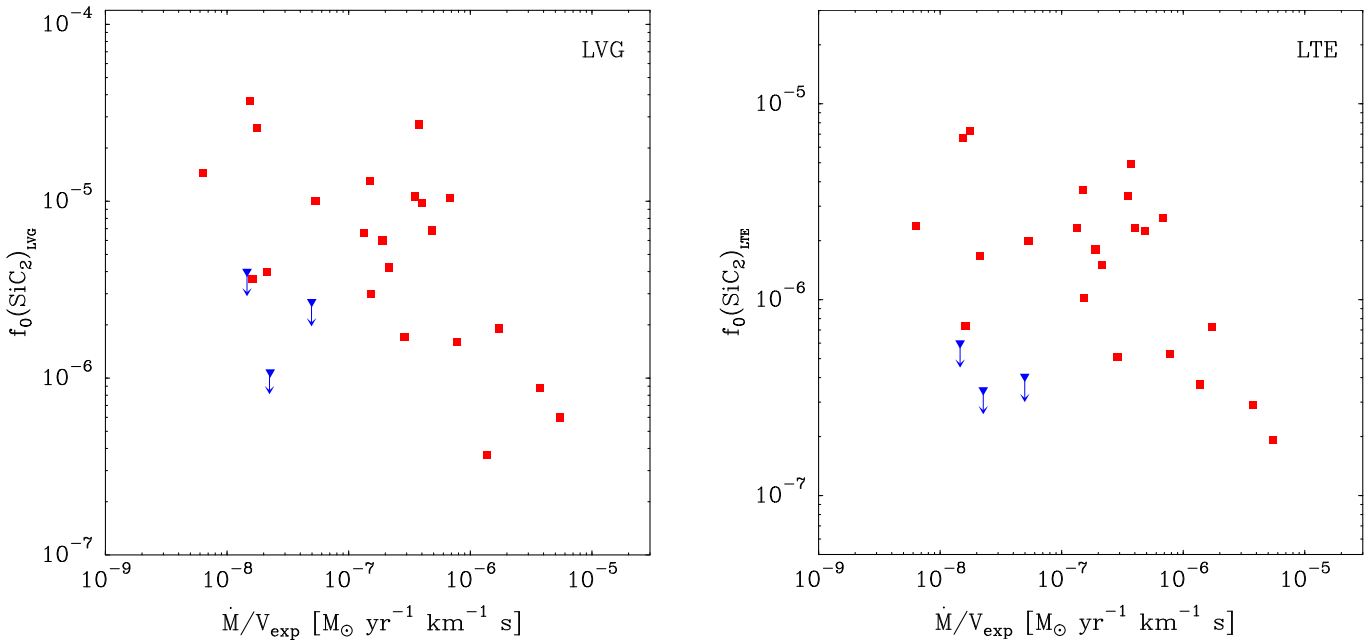

Fig. 6. Fractional abundances of SiC_2 (f_0) derived with the LVG method (*left panel*) and assuming LTE excitation (*right panel*) vs. the envelope density proxy $\dot{M}/V_{exp}$ for the 25 C-rich envelopes studied here. Blue downward triangles represent upper limits for f_0.

becomes less abundant as the density in the envelope increases. This trend is also present when the abundances derived assuming LTE are used. At this point, it is worth noting that the SiC_2 abundances derived in this work correspond to intermediate regions of the envelope. In a standard scenario describing the chemistry of an expanding envelope around an AGB star, the abundance with which a molecule is injected into the intermediate and outer envelope is set by the processes occurring in the inner regions. In this sense, the abundance of SiC_2 in the intermediate regions of the envelope is set by thermochemical equilibrium (TE) at the stellar surface and is possibly modified, i.e., driven out of thermochemical equilibrium, later on during the expansion by processes such as the formation of dust grains, shocks driven by the stellar pulsation, or even photochemical processes (e.g., Agúndez et al. 2010; Cherchneff 2012). The observational finding of a decrease in the SiC_2 abundance with increasing gas density can therefore be interpreted in different ways.

The observational trend could simply be a consequence of the way in which the TE abundance of SiC_2 depends on the density. To evaluate whether this could be a plausible explanation, we carried out thermochemical equilibrium calculations using the radial profiles of density and temperature of IRC +10216 (Agúndez et al. 2012; see downward revision on the density profile by Cernicharo et al. 2013) and scaling the density profile down or up depending on the mass-loss rate. In Fig. 7 we show the resulting TE abundance of SiC_2 within the first 10 R_* around the star for mass-loss rates between 10^{-7} and 10^{-4} $M_\odot$ yr^{-1}. In the region where SiC_2 reaches its maximum TE abundance, between 2 and 5 R_*, the abundance of SiC_2 is not very sensitive to the density. Outside this region the abundance of SiC_2 shows a marked dependence on density. At radii <2 R_*, SiC_2 becomes more abundant with increasing density (contrary to the observational trend), while beyond 5 R_* the SiC_2 abundance increases with decreasing density (as observed). At radii larger than 5 R_*, however, the TE abundance of SiC_2 experiences a drastic decline to values well below those observed, and thus it is unlikely that such regions set the abundance that is injected into the expanding envelope. Although it is difficult to precisely locate the region where molecular abundances, in general, and

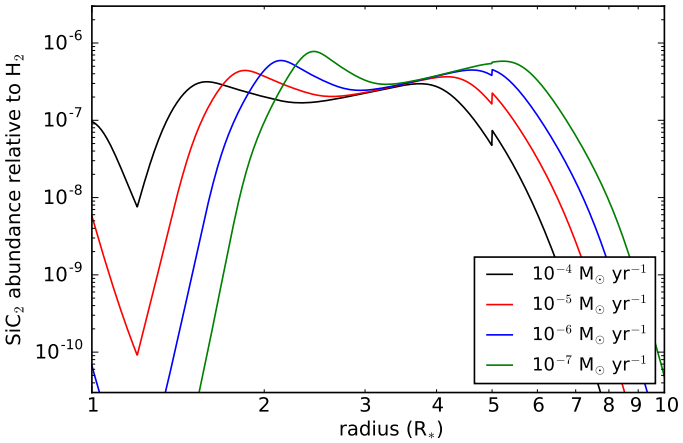

Fig. 7. Calculated fractional abundance of SiC_2 at thermochemical equilibrium as a function of distance to the star for various radial density profiles corresponding to mass-loss rates in the range 10^{-7}–10^{-4} $M_\odot$ yr^{-1}.

that of SiC_2 in particular, quench to the TE value, such a region should be located around 2–3 R_* (Agúndez & Cernicharo 2006; Agúndez et al. 2012), i.e., near the region where SiC_2 abundance is maximum and nearly insensitive to the density. We thus conclude that it is unlikely that the observational trend shown in Fig. 6 is caused by thermochemical equilibrium.

It therefore seems that the observational finding of a decline in the SiC_2 abundance with increasing density is caused by some nonequilibrium process that takes place beyond the region where thermochemical equilibrium holds. The most natural explanation is that SiC_2 molecules deplete from the gas phase to incorporate into solid dust grains, a process that is favored at higher densities owing to the higher rate at which collisions between particles occur. We stress that since the SiC_2 abundances derived here correspond to intermediate regions of the envelope where dust formation has already taken place, they have to be considered as post-condensation abundances. Further support for this scenario comes from mm-wave interferometric observations

of SiC_2 in the C-star envelope IRC +10216 (Lucas et al. 1995; Fonfría et al. 2014; Velilla Prieto et al. 2015), which shows that SiC_2 is present in regions close to the star, then experiences a marked abundance decline at 10−20 R_* (very likely due to condensation onto dust grains), and appears again in the outer envelope (probably as a result of the interaction between the UV radiation field and the envelope).

In order to further evaluate the hypothesis that the decline in the abundance of SiC_2 with increasing envelope density is caused by a more efficient incorporation of SiC_2 on silicon carbide dust, we collected information on infrared IRAS and ISO data for the sources in our sample that exhibit the SiC dust emission feature at 11.3 μm. Among the 25 sources in our sample, for 15 of them Sloan et al. (1998) have analyzed the IRAS LRS spectra and for 9 of them Yang et al. (2004) have studied the ISO SWS spectra. These authors determine the relative flux of SiC dust as the ratio of the integrated flux of the 11.3 μm emission feature (after continuum substraction) divided by the integrated flux of the continuum[4]. In Fig. 8 we plot the relative integrated flux of SiC dust vs. the fractional abundance of SiC_2 for the sources in our sample which have IRAS or ISO data. If the relative flux of SiC dust is a good proxy of the amount of silicon carbide dust, and if the hypothesis that SiC_2 is a gas-phase precursor of SiC dust is correct, one would expect to see a trend where the relative flux of SiC dust increases as the gas-phase abundance of SiC_2 decreases. This trend is not visible in Fig. 8. We note, however, that the relative flux of the 11.3 μm SiC band is an observable quantity that may not necessarily be a good proxy of the mass of silicon carbide dust in the envelope, the derivation of which requires a detailed radiative transfer analysis that includes a thorough description of the chemical composition and temperature of dust throughout the envelope. At this point, it therefore remains inconclusive whether or not there is a clear observational relation between the abundances of SiC_2 gas and SiC dust in C-rich envelopes. We plan to address this issue in a future study.

The question of identifying the main gas-phase precursors of dust grains in the ejecta of AGB stars has been, and continues to be, an exciting scientific topic. The problem has been addressed from different perspectives, mainly in the context of oxygen-rich AGB stars. For example, in a series of studies the abundance of SiO has been investigated in detail in a wide sample of envelopes around M stars (González Delgado et al. 2003), C stars (Schöier et al. 2006), and stars of S type (Ramstedt et al. 2009). Results from these studies show a clear trend of SiO becoming less abundant as the density of the envelope increases, a similar behavior to that found in this work for SiC_2 in C-rich envelopes. The observed trend for SiO has been also interpreted in terms of a more efficient adsorption of SiO onto dust grains for high envelope densities. It has been noted, however, that in the case of S stars, the trend is not as clear as in M and C stars, although this may be due to the low number of high mass-loss S stars observed (see Ramstedt et al. 2009). A similar study carried out on the abundance of SiS in envelopes around O- and C-rich stars (Schöier et al. 2007) did not find a clear correlation between the fractional abundance of SiS and the density of the envelope, suggesting that this molecule is not affected as much as SiO by freeze-out onto dust grains. The conclusions regarding SiS, however, are limited by the low number of O- and C-rich stars studied.

[4] The main difference between the two studies lies in the integration range, which is 7.67−14.03 μm for the IRAS spectra and 9−13.6 μm for the ISO data. For the sources that were observed with both telescopes, the main causes of the differences between the IRAS and ISO relative fluxes of SiC dust are the different integration ranges and the specific error in the spectra taken by each telescope.

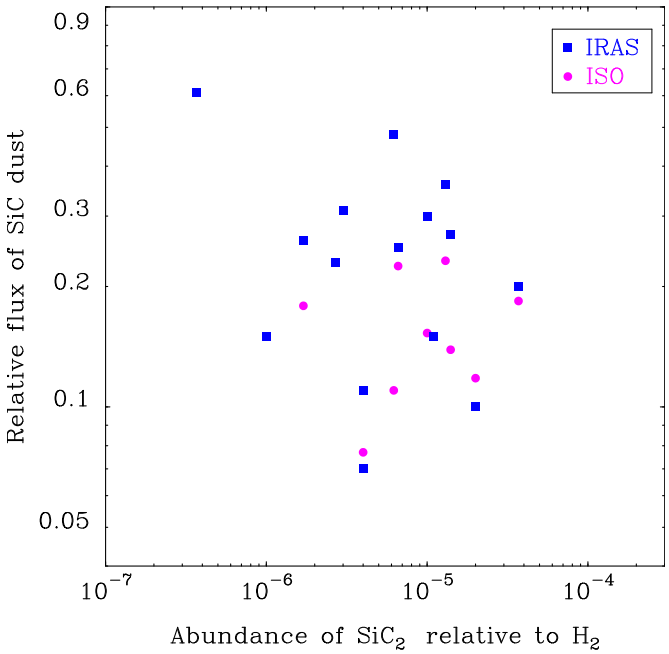

Fig. 8. Relative integrated flux of the SiC dust feature at 11.3 μm taken from the literature vs. the fractional abundance of SiC_2 derived in this work.

In a recent study, Liu & Jiang (2017) investigated the relation between the intensities of SiO maser and silicate dust emission in a sample of O-rich AGB and post-AGB stars in an attempt to relate the abundance of SiO, a highly plausible gas-phase precursor of silicates, with the amount of silicate dust. These authors find a positive correlation between the velocity-integrated intensity of SiO maser and the emission power of silicate dust, which is not against the hypothesis that SiO is a gas-phase precursor of silicate dust. It is important to note that in envelopes around O-rich AGB stars, SiO masers probe inner regions to where dust forms (Reid & Menten 1997; Danchi et al. 1994), and thus the more abundant the precursor SiO in the maser formation region is, the higher the amount of silicate dust can later be formed. In any case, given the peculiar nature of maser emission (e.g., Gray et al. 2009) and the fact that the observables are not a straightforward proxy of abundances, it is not clear whether the observed trend can be interpreted in terms of a higher fractional abundance of SiO in envelopes with a higher amount of silicate dust.

Various studies carried out in recent years have used ALMA to investigate the potential role of titanium and aluminum oxides as gas-phase precursors of inorganic dust in oxygen-rich evolved stars. In M stars, TiO_2 and Al_2O_3 are predicted to be among the first solid compounds to condense out of the gas phase (Gail & Sedlmayr 1998) and thus are ideal candidates to initiate the dust formation process. De Beck et al. (2015) and more recently Kamiński et al. (2017) have observed TiO and TiO_2 in the surroundings of the evolved stars VY Canis Majoris and Mira and found that these molecules extend out to several stellar radii from the star, and thus are unlikely to act as gas-phase precursors of TiO_2 dust. In a similar study, Kamiński et al. (2016) observed AlO around the star Mira, although they could not quantitatively assess the role of AlO as a gas-phase precursor of Al_2O_3 dust. ALMA is indeed a very promising tool for identifying gas-phase precursors of dust in evolved stars, but results are still not conclusive.

7. Conclusions

In this work we used the IRAM 30 m telescope to survey a sample of 25 C-rich circumstellar envelopes and search for rotational emission from the molecules SiC_2, SiC, and Si_2C. We detected SiC_2 in most of the sources and SiC in about half of them, while Si_2C was not detected in any of the sources with the exception of IRC +10216. We carried out excitation and radiative transfer calculations to derive SiC_2 fractional abundances. We found a clear trend in which SiC_2 becomes less abundant as the envelope density increases. We interpret this result as evidence of efficient incorporation of SiC_2 onto dust grains, a process that is more efficient at high densities because collisions between particles and coagulation processes become faster. The ring molecule SiC_2 thus emerges as a very likely gas-phase precursor in the process of formation of SiC dust in envelopes around C-rich AGB stars; therefore, SiC_2 seems to behave similarly to SiO, which has been found to deplete from the gas phase as the density in the envelope increases. The search for the gas-phase building blocks of dust grains in both carbon- and oxygen-rich AGB stars is a challenging scientific objective, in which astronomical observations still have to provide many answers. Observing other molecules containing refractory elements is necessary in order to understand which of the gas-phase molecules that are present in the atmospheres of AGB stars serve as precursor material to feed the process of dust grain formation.

Acknowledgements. We thank the IRAM 30 m staff for their help during the observations. This research has made use of the SIMBAD database, operated at CDS, Strasbourg, France. We acknowledge funding support from the European Research Council (ERC Grant 610256: NANOCOSMOS) and from Spanish MINECO through grants AYA2012-32032 and AYA2016-75066-C2-1-P. M.A. thanks Spanish MINECO for funding support through the Ramón y Cajal programme (RyC-2014-16277).

References

Agúndez, M., & Cernicharo, J. 2006, ApJ, 650, 374
Agúndez, M., Cernicharo, J., & Guélin, M. 2010, ApJ, 724, L133
Agúndez, M., Fonfría, J. P., Cernicharo, J., et al. 2012, A&A, 543, A48
Agúndez, M., Cernicharo, J., & Guélin, M. 2014, A&A, 570, A45
Agúndez, M., Cernicharo, J., Quintana-Lacaci, G., et al. 2017, A&A, 601, A4
Apponi, A. J., McCarthy, M. C., Gottlieb, C. A., & Thaddeus, P. 1999, ApJ, 516, L103
Asplund, M., Grevesse, N., Sauval, A. J., & Scott, P. 2009, ARA&A, 47, 481
Bachiller, R., Forveille, T., Huggins, P. J., & Cox, P. 1997, A&A, 324, 1123
Bohlin, R. C., Savage, B. D., & Drake, J. F. 1978, ApJ, 224, 132
Bujarrabal, V., Fuente, A., & Omont, A. 1994, A&A, 285, 247
Cernicharo, J. 1985, IRAM Internal Report, 52
Cernicharo, J., Gottlieb, C. A., Guelin, M., Thaddeus, P., & Vrtilek, J. M. 1989, ApJ, 341, L25
Cernicharo, J., Yamamura, I., González-Alfonso, E., et al. 1999, ApJ, 526, L41
Cernicharo, J., Guélin, M., & Kahane, C. 2000, A&AS, 142, 181
Cernicharo, J., Waters, L. B. F. M., Decin, L., et al. 2010, A&A, 521, L8
Cernicharo, J., Daniel, F., Castro-Carrizo, A., et al. 2013, ApJ, 778, L25
Cernicharo, J., Teyssier, D., Quintana-Lacaci, G., et al. 2014, ApJ, 796, L21
Cernicharo, J., Marcelino, N., Agúndez, M., & Guélin, M. 2015a, A&A, 575, A91
Cernicharo, J., McCarthy, M. C., Gottlieb, C. A., et al. 2015b, ApJ, 806, L3
Cernicharo, J., Agúndez, M., Velilla Prieto, L., et al. 2017, A&A, 606, L5
Chan, S. J., & Kwok, S. 1990, A&A, 237, 354
Chandra, S., & Kegel, W. H. 2000, A&AS, 142, 113
Cherchneff, I. 2012, A&A, 545, A12
Cordiner, M. A., & Millar, T. J. 2009, ApJ, 697, 68
Danchi, W., Bester, M., Degiacomi, C. G., Greenhill, L., & Townes, C. 1994, AJ, 107, 1469
Danilovich, T., Teyssier, D., Justtanont, K., et al. 2015, A&A, 581, A60
De Beck, E., Decin, L., de Koter, A., et al. 2010, A&A, 523, A18
De Beck, E., Lombaert, R., Agúndez, M., et al. 2012, A&A, 539, A108
De Beck, E., Vlemmings, W., Muller, S., et al. 2015, A&A, 580, A36
Fonfría, J. P., Fernández-López, M., Agúndez, M., et al. 2014, MNRAS, 445, 3289
Gail, H.-P., & Sedlmayr, E. 1998, Faraday Discussions, 109, 303
Gail, H.-P., Keller, R., & Sedlmayr, E. 1984, A&A, 133, 320
Gehrz, R. 1989, in Interstellar Dust, eds. L. J. Allamandola, & A. G. G. M. Tielens, IAU Symp., 135, 445
González Delgado, D., Olofsson, H., Kerschbaum, F., et al. 2003, A&A, 411, 123
Gray, M., Wittkowski, M., Scholz, M., et al. 2009, MNRAS, 394, 51
Green, S. 1995, ApJS, 100, 213
Groenewegen, M. A. T., Baas, F., de Jong, T., & Loup, C. 1996, A&A, 306, 241
Groenewegen, M. A. T., Whitelock, P. A., Smith, C. H., & Kerschbaum, F. 1998, MNRAS, 293, 18
Groenewegen, M. A. T., Sevenster, M., Spoon, H. W. W., & Pérez, I. 2002, A&A, 390, 511
Guandalini, R., & Cristallo, S. 2013, A&A, 555, A120
Guandalini, R., Busso, M., Ciprini, S., Silvestro, G., & Persi, P. 2006, A&A, 445, 1069
Guélin, M., Muller, S., Cernicharo, J., et al. 2000, A&A, 363, L9
Guélin, M., Patel, N. A., Bremer, M., et al. 2018, A&A, 610, A4
Hackwell, J. A. 1972, A&A, 21, 239
Hammami, K., Lique, F., Jaïdane, N., et al. 2007, A&A, 462, 789
Huggins, P. J., & Glassgold, A. E. 1982, ApJ, 252, 201
Jura, M., & Morris, M. 1981, ApJ, 251, 181
Kamiński, T., Wong, K. T., Schmidt, M. R., et al. 2016, A&A, 592, A42
Kamiński, T., Müller, H. S. P., Schmidt, M. R., et al. 2017, A&A, 599, A59
Kerschbaum, F., Charbonnel, C., & Wing, R. F. 2007, Why Galaxies Care About AGB Stars: Their Importance as Actors and Probes, ASP Conf. Ser., 378
Little-Marenin, I. R. 1986, ApJ, 307, L15
Liu, J., & Jiang, B. 2017, AJ, 153, 176
Loup, C., Forveille, T., Omont, A., & Paul, J. F. 1993, A&AS, 99, 291
Lucas, R., Guélin, M., Kahane, C., Audinos, P., & Cernicharo, J. 1995, Ap&SS, 224, 293
MacKay, D. D. S., & Charnley, S. B. 1999, MNRAS, 302, 793
Mauron, N., & Huggins, P. J. 2000, A&A, 359, 707
Müller, H. S. P., Cernicharo, J., Agúndez, M., et al. 2012, J. Mol. Spectr., 271, 50
Nyman, L.-A., Olofsson, H., Johansson, L. E. B., et al. 1993, A&A, 269, 377
Ohishi, M., Kaifu, N., Kawaguchi, K., et al. 1989, ApJ, 345, L83
Olofsson, H., Eriksson, K., Gustafsson, B., & Carlstrom, U. 1993, ApJS, 87, 267
Pardo, J. R., Cernicharo, J., & Serabyn, E. 2001, IEEE Transactions on Antennas and Propagation, 49, 1683
Patel, N. A., Young, K. H., Gottlieb, C. A., et al. 2011, ApJS, 193, 17
Ramstedt, S., & Olofsson, H. 2014, A&A, 566, A145
Ramstedt, S., Schöier, F. L., & Olofsson, H. 2009, A&A, 499, 515
Reid, M. J., & Menten, K. M. 1997, AJ, 476, 327
Sánchez Contreras, C., & Sahai, R. 2012, ApJS, 203, 16
Sarre, P. J., Hurst, M. E., & Lloyd Evans, T. 2000, MNRAS, 319, 103
Schöier, F. L., & Olofsson, H. 2001, A&A, 368, 969
Schöier, F. L., Lindqvist, M., & Olofsson, H. 2005, A&A, 436, 633
Schöier, F. L., Olofsson, H., & Lundgren, A. A. 2006, A&A, 454, 247
Schöier, F. L., Bast, J., Olofsson, H., & Lindqvist, M. 2007, A&A, 473, 871
Schöier, F. L., Ramstedt, S., Olofsson, H., et al. 2013, A&A, 550, A78
Skinner, C. J., Justtanont, K., Tielens, A. G. G. M., et al. 1999, MNRAS, 302, 293
Sloan, G. C., Little-Marenin, I. R., & Price, S. D. 1998, AJ, 115, 809
Speck, A. K., Corman, A. B., Wakeman, K., Wheeler, C. H., & Thompson, G. 2009, ApJ, 691, 1202
Suenram, R. D., Lovas, F. J., & Matsumura, K. 1989, ApJ, 342, L103
Suh, K.-W. 2000, MNRAS, 315, 740
Swamy, K. K. 2005, Dust in the universe: similarities and differences (World Scientific), 7
Tejero, J., & Cernicharo, J. 1991, Modelos de Equilibrio Termodinámico Aplicados a Envolturas Circunestelares de Estrellas Evolucionadas (Madrid: IGN)
Thaddeus, P., Cummins, S. E., & Linke, R. A. 1984, ApJ, 283, L45
Treffers, R., & Cohen, M. 1974, ApJ, 188, 545
Velilla Prieto, L., Cernicharo, J., Quintana-Lacaci, G., et al. 2015, ApJ, 805, L13
Wenger, M., Ochsenbein, F., Egret, D., et al. 2000, A&AS, 143, 9
Yang, X., Chen, P., & He, J. 2004, A&A, 414, 1049
Yasuda, Y., & Kozasa, T. 2012, ApJ, 745, 159
Zhang, Y., Kwok, S., & Dinh-V-Trung. 2009a, ApJ, 691, 1660
Zhang, Y., Kwok, S., & Nakashima, J.-i. 2009b, ApJ, 700, 1262

Appendix A

Table A.1. Observed line parameters of SiC_2.

Line	ν_{calc} (MHz)	ν_{obs} (MHz)	V_e (km s^{-1})	$\int T_A^* dv$ (K km s^{-1})
		IRC +10216		
$6_{2,5}-5_{2,4}$	140920.171	140920.1(1)	13.8(1)	41.2(4)
$6_{4,3}-5_{4,2}$	141751.492	141751.3(1)	13.8(1)	21.5(2)[a]
$6_{4,2}-5_{4,1}$	141755.360	141755.2(1)	13.8(1)	22.2(2)[a]
$6_{2,4}-5_{2,3}$	145325.875	145325.8(1)	14.3(1)	42.4(4)
$7_{0,7}-6_{0,6}$	158499.228	158499.1(1)	15.3(1)	58.7(5)
		CIT 6		
$6_{2,5}-5_{2,4}$	140920.171	140920.5(10)	16.2(8)	8.2(8)
$6_{4,3}-5_{4,2}$	141751.492	141751.1(2)	15.4(8)	5.4(5)[a]
$6_{4,2}-5_{4,1}$	141755.360	141754.9(3)	14.0(8)	2.7(3)[a]
$6_{2,4}-5_{2,3}$	145325.875	145325.0(10)	13.8(10)	8.0(8)
$7_{0,7}-6_{0,6}$	158499.228	158498.5(10)	15.1(8)	12.9(13)
		CRL 3068		
$6_{2,5}-5_{2,4}$	140920.171	140920.5(1)	12.8(8)	1.78(2)
$6_{4,3}-5_{4,2}$	141751.492	141751.3(1)	12.8(4)	1.07(1)[a]
$6_{4,2}-5_{4,1}$	141755.360	141755.3(1)	12.8(4)	1.02(1)[a]
$6_{2,4}-5_{2,3}$	145325.875	145325.7(1)	13.2(6)	1.84(2)
$7_{0,7}-6_{0,6}$	158499.228	158499.2(2)	14.5(8)	2.73(3)
		S Cep		
$6_{2,5}-5_{2,4}$	140920.171	140920.3(5)	20.5(4)	0.94(9)
$6_{4,3}-5_{4,2}$	141751.492	141751.3(5)	21.8(1)	0.63(6)[a]
$6_{4,2}-5_{4,1}$	141755.360	141755.9(5)	22.4(1)	0.49(5)[a]
$6_{2,4}-5_{2,3}$	145325.875	145325.5(5)	21.7(8)	1.06(10)
$7_{0,7}-6_{0,6}$	158499.228	158499.9(2)	23.0(5)	1.66(16)
		IRC +30374		
$6_{2,5}-5_{2,4}$	140920.171	140920.4(1)	23.0(8)	1.43(14)
$6_{4,3}-5_{4,2}$	141751.492	141751.8(3)	22.8(4)	0.84(8)[a]
$6_{4,2}-5_{4,1}$	141755.360	141755.5(3)	22.9(4)	0.62(6)[a]
$6_{2,4}-5_{2,3}$	145325.875	145325.9(1)	23.4(4)	1.50(4)
$7_{0,7}-6_{0,6}$	158499.228	158499.4(1)	25.5(8)	2.22(2)
		Y CVn		
$6_{2,5}-5_{2,4}$	140920.171	140921.7(10)	8.6(10)	0.23(4)
$6_{4,3}-5_{4,2}$	141751.492	141751.7(2)	7.3(8)	0.16(2)[a]
$6_{4,2}-5_{4,1}$	141755.360	141755.7(2)	7.5(6)	0.12(2)[a]
$6_{2,4}-5_{2,3}$	145325.875	145326.3(10)	7.1(10)	0.26(5)
$7_{0,7}-6_{0,6}$	158499.228	158499.1(5)	6.6(5)	0.44(9)
		LP And		
$6_{2,5}-5_{2,4}$	140920.171	140920.3(1)	13.0(8)	3.86(4)
$6_{4,3}-5_{4,2}$	141751.492	141751.6(2)	13.1(8)	1.93(2)[a]
$6_{4,2}-5_{4,1}$	141755.360	141755.4(2)	13.2(8)	2.06(2)[a]
$6_{2,4}-5_{2,3}$	145325.875	145325.9(1)	13.4(8)	3.99(4)
$7_{0,7}-6_{0,6}$	158499.228	158499.3(1)	14.6(8)	6.34(6)
		V Cyg		
$6_{2,5}-5_{2,4}$	140920.171	140920.3(1)	10.4(8)	1.87(2)
$6_{4,3}-5_{4,2}$	141751.492	141751.7(2)	10.8(4)	0.91(2)[a]
$6_{4,2}-5_{4,1}$	141755.360	141755.4(2)	10.6(4)	0.91(2)[a]
$6_{2,4}-5_{2,3}$	145325.875	145326.1(3)	11.0(8)	1.95(2)
$7_{0,7}-6_{0,6}$	158499.228	158499.4(1)	11.8(8)	3.47(3)

Notes. Numbers in parentheses are 1σ uncertainties in units of the last digits. [(a)] Blend of two lines, each of which could be fitted individually. [(b)] Blend of two lines which could not be fitted individually. Only one component was fitted. [(c)] Marginal detection.

Table A.1. continued.

Line	ν_{calc} (MHz)	ν_{obs} (MHz)	V_e (km s^{-1})	$\int T_A^* dv$ (K km s^{-1})
		V384 Per		
$6_{2,5}-5_{2,4}$	140920.171	140920.2(1)	13.5(4)	1.80(2)
$6_{4,3}-5_{4,2}$	141751.492	141751.4(1)	13.9(2)	0.80(1)[a]
$6_{4,2}-5_{4,1}$	141755.360	141755.1(1)	13.8(2)	1.04(2)[a]
$6_{2,4}-5_{2,3}$	145325.875	145326.0(1)	13.6(8)	1.88(2)
$7_{0,7}-6_{0,6}$	158499.228	158499.3(1)	15.1(1)	3.09(3)
		IRC +60144		
$6_{2,5}-5_{2,4}$	140920.171	140920.4(5)	19.1(8)	0.55(5)
$6_{4,3}-5_{4,2}$	141751.492	141751.3(1)	18.5(2)	0.37(4)[a]
$6_{4,2}-5_{4,1}$	141755.360	141755.4(4)	19.9(3)	0.25(2)[a]
$6_{2,4}-5_{2,3}$	145325.875	145325.9(2)	19.7(1)	0.25(2)
$7_{0,7}-6_{0,6}$	158499.228	158499.4(2)	21.5(4)	0.73(7)
		U Cam		
$6_{2,5}-5_{2,4}$	140920.171	140920.8(5)	11.2(5)	0.39(4)
$6_{4,3}-5_{4,2}$	141751.492	141751.9(10)	14.0(8)	0.21(2)[a]
$6_{4,2}-5_{4,1}$	141755.360	141755.5(10)	13.1(8)	0.19(2)[a]
$6_{2,4}-5_{2,3}$	145325.875	145326.3(10)	11.9(8)	0.41(4)
$7_{0,7}-6_{0,6}$	158499.228	158499.6(5)	12.6(5)	0.63(6)
		V636 Mon		
$6_{2,5}-5_{2,4}$	140920.171	140921.2(10)	21.3(10)	0.35(7)
$6_{4,3}-5_{4,2}$	141751.492	141751.8(4)	20.3(8)	0.17(3)[a]
$6_{4,2}-5_{4,1}$	141755.360	141754.4(3)	19.7(6)	0.23(5)[a]
$6_{2,4}-5_{2,3}$	145325.875	145326.5(10)	23.3(10)	0.37(1)
$7_{0,7}-6_{0,6}$	158499.228	158499.9(10)	21.8(10)	0.61(2)
		IRC +20370		
$6_{2,5}-5_{2,4}$	140920.171	140920.2(1)	13.0(2)	0.98(9)
$6_{4,3}-5_{4,2}$	141751.492	141751.6(5)	13.2(5)	0.53(5)[a]
$6_{4,2}-5_{4,1}$	141755.360	141755.3(5)	13.4(5)	0.51(5)[a]
$6_{2,4}-5_{2,3}$	145325.875	145325.9(3)	13.2(5)	1.12(11)
$7_{0,7}-6_{0,6}$	158499.228	158499.3(2)	14.6(1)	1.83(18)
		W Ori		
$6_{2,5}-5_{2,4}$	140920.171	140920.2(10)	9.4(10)	0.12(5)[c]
$6_{4,3}-5_{4,2}$	141751.492	141751.5(10)	10.5(10)	0.06(1)[c]
$6_{4,2}-5_{4,1}$	141755.360	141754.6(10)	10.9(10)	0.06(3)[c]
$6_{2,4}-5_{2,3}$	145325.875	145325.2(10)	8.2(10)	0.11(2)[c]
$7_{0,7}-6_{0,6}$	158499.228	158499.9(5)	12.1(10)	0.31(6)
		CRL 67		
$6_{2,5}-5_{2,4}$	140920.171	140920.3(1)	14.6(1)	1.57(1)
$6_{4,3}-5_{4,2}$	141751.492	141751.5(5)	15.6(5)	0.72(7)[a]
$6_{4,2}-5_{4,1}$	141755.360	141755.2(5)	14.9(5)	0.96(9)[a]
$6_{2,4}-5_{2,3}$	145325.875	145325.9(2)	14.6(4)	1.61(2)
$7_{0,7}-6_{0,6}$	158499.228	158499.3(3)	15.8(4)	2.47(2)
		CRL 190		
$6_{2,5}-5_{2,4}$	140920.171	140920.6(1)	16.4(1)	1.08(10)
$6_{4,3}-5_{4,2}$	141751.492	141751.6(3)	16.3(5)	0.29(3)[a]
$6_{4,2}-5_{4,1}$	141755.360	141755.1(2)	15.2(5)	0.37(4)[a]
$6_{2,4}-5_{2,3}$	145325.875	145325.9(1)	15.4(1)	0.12(1)
$7_{0,7}-6_{0,6}$	158499.228	158499.6(1)	16.8(4)	0.77(7)
		S Aur		
$6_{2,5}-5_{2,4}$	140920.171	140920.3(10)	23.7(10)	0.11(2)[c]
$6_{4,3}-5_{4,2}$	141751.492	141753.1(10)	22.2(14)	0.13(3)[b,c]
$6_{4,2}-5_{4,1}$	141755.360	–	–	–
$6_{2,4}-5_{2,3}$	145325.875	145324.9(10)	25.7(15)	0.15(3)[c]
$7_{0,7}-6_{0,6}$	158499.228	158499.1(5)	24.4(8)	0.28(6)

Table A.1. continued.

Line	ν_{calc} (MHz)	ν_{obs} (MHz)	V_e (km s^{-1})	$\int T_A^* dv$ (K km s^{-1})
		V Aql		
$6_{2,5}-5_{2,4}$	140920.171	140920.1(5)	6.7(4)	0.31(6)
$6_{4,3}-5_{4,2}$	141751.492	141751.7(10)	8.0(10)	0.26(5)[b]
$6_{4,2}-5_{4,1}$	141755.360	141755.3(10)	9.7(10)	0.12(2)[b]
$6_{2,4}-5_{2,3}$	145325.875	145326.1(5)	8.1(6)	0.38(7)
$7_{0,7}-6_{0,6}$	158499.228	158499.2(5)	8.0(5)	0.60(12)
		CRL 2513		
$6_{2,5}-5_{2,4}$	140920.171	140922.1(10)	20.3(10)	0.22(4)
$6_{4,3}-5_{4,2}$	141751.492	141751.7(10)	20.6(10)	0.23(4)[b]
$6_{4,2}-5_{4,1}$	141755.360	–	–	–
$6_{2,4}-5_{2,3}$	145325.875	145326.3(10)	25.6(10)	0.29(6)[c]
$7_{0,7}-6_{0,6}$	158499.228	158499.8(5)	26.9(4)	0.58(11)
		CRL 2477		
$6_{2,5}-5_{2,4}$	140920.171	140920.1(1)	18.5(10)	0.46(4)
$6_{4,3}-5_{4,2}$	141751.492	141751.5(2)	18.2(4)	0.28(6)[a]
$6_{4,2}-5_{4,1}$	141755.360	141755.2(2)	19.9(4)	0.30(6)[a]
$6_{2,4}-5_{2,3}$	145325.875	145325.7(5)	19.3(5)	0.51(1)
$7_{0,7}-6_{0,6}$	158499.228	158499.5(5)	20.0(5)	0.72(14)
		CRL 2494		
$6_{2,5}-5_{2,4}$	140920.171	140920.2(5)	17.4(8)	1.41(1)
$6_{4,3}-5_{4,2}$	141751.492	141751.8(5)	18.1(5)	0.81(1)[a]
$6_{4,2}-5_{4,1}$	141755.360	141755.3(5)	18.1(5)	0.91(1)[a]
$6_{2,4}-5_{2,3}$	145325.875	145326.7(5)	18.3(8)	1.53(1)
$7_{0,7}-6_{0,6}$	158499.228	158499.5(3)	19.5(4)	2.10(2)
		RV Aqr		
$6_{2,5}-5_{2,4}$	140920.171	140920.7(10)	14.3(10)	0.37(7)
$6_{4,3}-5_{4,2}$	141751.492	141751.4(5)	14.7(10)	0.18(3)[a]
$6_{4,2}-5_{4,1}$	141755.360	141755.3(5)	14.2(10)	0.18(3)[a]
$6_{2,4}-5_{2,3}$	145325.875	145325.9(10)	15.6(10)	0.39(8)
$7_{0,7}-6_{0,6}$	158499.228	158499.6(5)	15.5(5)	0.65(10)

Table A.2. Observed parameters of the SiC $^3\Pi_2$ $J = 4-3$ line.

Source	ν_{calc} (MHz)	ν_{obs} (MHz)	V_e (km s^{-1})	$\int T_A^* dv$ (K km s^{-1})
IRC +10216	157494.101	157494.1(1)	15.4(8)	5.86(6)
CIT 6	157494.101	157493.2(10)	15.4(8)	0.96(9)
CRL 3068	157494.101	157494.2(5)	15.7(5)	0.29(6)
IRC +30374	157494.101	157495.5(10)	25.1(10)	0.18(3)[a]
LP And	157494.101	157493.8(5)	14.4(4)	0.56(6)
V Cyg	157494.101	157496.3(10)	11.3(10)	0.11(2)[a]
V384 Per	157494.101	157493.7(10)	15.2(10)	0.17(3)[a]
IRC +60144	157494.101	157492.8(10)	20.2(10)	0.12(6)[a]
IRC +20370	157494.101	157494.3(10)	15.8(10)	0.13(2)[a]
CRL 67	157494.101	157494.8(10)	16.6(10)	0.28(6)[a]
CRL 2477	157494.101	157493.7(10)	18.7(10)	0.10(2)[a]
CRL 2494	157494.101	157493.5(10)	21.8(10)	0.23(4)[a]

Notes. Numbers in parentheses are 1σ uncertainties in units of the last digits. [(a)] Marginal detection.